nature materials

Article

https://doi.org/10.1038/s41563-026-02768-3

Single-stripe magnetic order and bilayer spin dynamics in single-crystalline $La_3Ni_2O_7$

Received: 4 May 2026

Accepted: 10 September 2026

Published online: 02 October 2026

Check for updates

Lixing Chen[1,8], Enkang Zhang[1,8], Yiqing Hao[2], Yinghao Zhu[1], Bingkun Cui[1], Douglas L. Abernathy[2], Travis J. Williams[3], Yoichi Ikeda[4], Hao Zhang[1], Feiyang Liu[1], Wenbin Wang[5], Qisi Wang[6] & Jun Zhao[1,5,7]

High-temperature superconductivity in pressurized and thin-film nickelates has generated intense interest, yet magnetism in their ambient-pressure parent phases remains poorly understood, despite its potentially crucial role in pairing. Progress has been limited by the lack of large single crystals suitable for neutron spectroscopy. Here we overcome this limitation and map the spin order and excitations of single-crystalline $La_3Ni_2O_7$. We find single-stripe magnetic order with a finite spin gap, anisotropic in-plane excitations and pronounced bilayer modulation revealing antiferromagnetic interlayer coupling. The dispersion is captured by a bilayer Heisenberg-type model with strong interlayer exchange and competing in-plane couplings. Absolute normalization reveals that, although the spin-wave bandwidth is only about 25% of that in cuprates, the local dynamic susceptibility at comparable energies is enhanced, yielding a comparable total fluctuating moment. These results highlight intense mid-energy spin excitations rooted in substantial electronic correlations, establishing a magnetic framework distinct from cuprates and relevant to superconductivity in nickelates.

Since the discovery of high-temperature cuprate superconductors nearly four decades ago, a central challenge has been to identify the interactions that mediate electron pairing. Because high-temperature superconductivity develops when static antiferromagnetic order in the parent compound is suppressed by carrier doping, magnetism is widely believed to play a pivotal role in the pairing mechanism[1–3]. However, despite decades of intensive research, the microscopic interactions that control high-temperature superconductivity have not yet been established conclusively.

High-temperature superconductivity in pressurized Ruddlesden–Popper nickelates[4,5] and in epitaxially strained nickelate thin films[6–8] offers a fresh perspective on unconventional pairing. Although nickelates have similar layered structural motifs as cuprates, they differ in their electronic configurations and orbital hierarchy[9]. In cuprates, the low-energy electronic structure is dominated by a single Cu $3d_{x^2-y^2}$ orbital, forming a nearly ideal two-dimensional antiferromagnetic state[1]. By contrast, Ruddlesden–Popper nickelates host mixed-valence Ni ions with $3d^7$ and $3d^8$ configurations, where both $d_{x^2-y^2}$ and d_{z^2} orbitals can contribute near the Fermi level[4,5]. The d_{z^2} orbital couples through apical oxygens, mediating interlayer correlation, whereas the $d_{x^2-y^2}$ orbital primarily governs in-plane correlations, as for cuprates. The participation of several orbitals can generate orbital-selective degrees of freedom, alter the underlying magnetic exchange pathways[10–16] and potentially lead to qualitatively different pairing interactions[17–30]. Such similarities and differences place nickelates at a unique crossroads between cuprates and other correlated

[1]State Key Laboratory of Surface Physics and Department of Physics, Fudan University, Shanghai, China. [2]Neutron Scattering Division, Oak Ridge National Laboratory, Oak Ridge, TN, USA. [3]ISIS Neutron and Muon Source, STFC Rutherford Appleton Laboratory, Didcot, UK. [4]Institute for Materials Research, Tohoku University, Sendai, Japan. [5]Institute of Nanoelectronics and Quantum Computing, Fudan University, Shanghai, China. [6]Department of Physics, The Chinese University of Hong Kong, Shatin, Hong Kong, China. [7]Shanghai Research Center for Quantum Sciences, Shanghai, China. [8]These authors contributed equally: Lixing Chen, Enkang Zhang. e-mail: zhaoj@fudan.edu.cn

https://doi.org/10.1038/s41563-026-02768-3

superconductors, offering an unprecedented opportunity to disentangle the intertwined roles of spin fluctuations and orbital character in high-critical temperature (T_c) superconductivity.

In particular, bilayer $La_3Ni_2O_7$ exhibits superconductivity under pressure or compressive epitaxial strain with transition temperatures reaching around 90 K, placing it among the highest T_c unconventional superconductors outside the cuprates[4,7,8,31]. At ambient conditions, $La_3Ni_2O_7$ develops antiferromagnetic order, establishing it as the parent compound of the pressurized or thin-film superconducting phases. Previous studies of resonant X-ray scattering on single crystals or thin films reported a magnetic Bragg peak at (0, 0.5, L) in the orthorhombic notation, corresponding to (0.25, 0.25, L) in the pseudotetragonal notation (Supplementary Fig. 9), consistent with either stripe or double-stripe order[32–35]. This is consistent with muon spin rotation and nuclear magnetic resonance measurements, which likewise detect static magnetism[36–38]. A recent synchrotron X-ray diffraction study further reported charge order with inequivalent Ni sites in $La_3Ni_2O_7$, highlighting the importance of charge disproportionation in this material[39]. Elastic neutron diffraction on powders identified a more complex situation: although some studies reported no magnetic order[40,41], others found two coexisting magnetic wavevectors, $\mathbf{q}$ = (0, 0.5, 0) and (0, 0.5, 0.5), suggesting possible phase separation[42]. Dynamically, resonant inelastic X-ray scattering from single crystals has revealed spin excitations that are compatible with either stripe or double-stripe scenarios[32], and the excitations in superconducting films under compressive strain[35] are rather like those in the bulk. This suggests that spin correlations relevant to pairing are already present in the parent phase, as for cuprates[43]. On the other hand, inelastic neutron scattering from polycrystalline samples identified only a weak flat spin-fluctuation signal near 45 meV (ref. 40). Both the resonant inelastic X-ray and neutron scattering results have been interpreted in terms of strong interlayer magnetic interactions. However, a complete picture of the momentum- and energy-resolved spin correlations across the entire Brillouin zone, including the low-energy spin gap, in-plane anisotropy, out-of-plane modulation, absolute local dynamic susceptibility, total fluctuating magnetic moment and the precise magnetic interactions and structure, remains to be established. Such information is essential for establishing the role of electron correlation and for constraining microscopic models of magnetism and superconductivity.

Progress in this field has long been hindered by the formidable challenge of synthesizing large $La_3Ni_2O_7$ single crystals suitable for advanced spectroscopic probes, such as neutron scattering. We overcame this bottleneck by optimizing high-pressure optical floating-zone growth, enabling the production of millimetre- to centimetre-sized crystals. This advance enabled us to map the magnetic correlations of $La_3Ni_2O_7$ over broad ranges of momentum and energy. Our measurements established single-stripe magnetic order, revealed strong antiferromagnetic coupling between the two NiO_2 layers of a bilayer and quantified both the competing in-plane interactions and the absolute spectral weight of the spin fluctuations. These results establish a quantitative magnetic framework for the ambient-pressure parent phase of superconducting bilayer nickelates.

We first characterized $La_3Ni_2O_7$ single crystals. Figure 1c shows a representative magnetic susceptibility curve with a clear anomaly near 151 K, marking the onset of a magnetic phase transition. Moreover, crystals from the same growth batch have been shown to exhibit robust superconductivity under pressure, characterized by sharp superconducting transitions, zero resistance and well-defined superconducting gaps[44].

To investigate the magnetic ordering, we performed neutron diffraction measurements. In contrast to previous studies on powder samples that reported either two sets of magnetic ordering peaks or no magnetic peaks at all, our single crystals display well-defined magnetic Bragg peaks corresponding to $\mathbf{q}$ = (0, 0.5, 0.5), with no evidence for peaks at $\mathbf{q}$ = (0, 0.5, 0) (Fig. 1d and Supplementary Fig. 2). This confirms the presence of a single magnetic phase without phase separation,

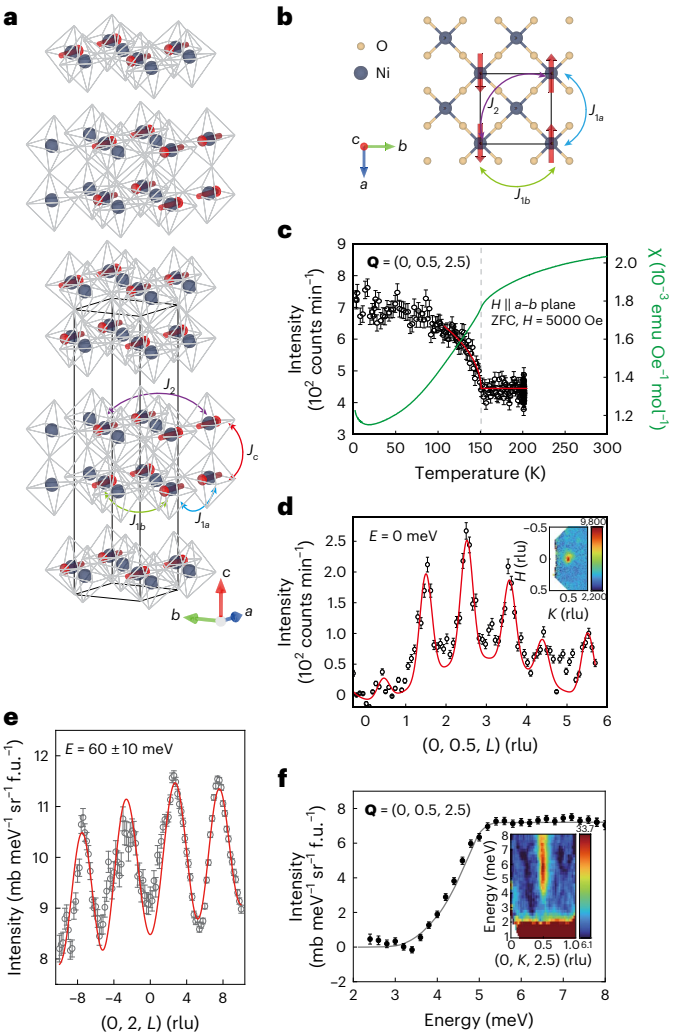


Fig. 1 | Magnetic structure, susceptibility and spin dynamics of $La_3Ni_2O_7$. **a**, Schematic illustration of the stripe-type magnetic structure. The moments on magnetic Ni ions and relevant exchange interactions are indicated in the figure. The unit cell is represented by a cuboid with dimensions a = 5.399 Å, b = 5.440 Å and c = 20.631 Å. For clarity, only Ni ions are shown. Red arrows denote the ordered moments on magnetic Ni sites. Non-magnetic Ni sites are drawn without arrows. **b**, Magnetic structure and exchange interactions within the NiO_2 plane. **c**, Temperature dependence of the zero-field-cooled (ZFC) magnetic susceptibility χ measured under an external magnetic field of 5,000 Oe applied parallel to the a–b plane, together with the magnetic order parameter obtained from neutron diffraction. The intensity of the magnetic Bragg peak (0, 0.5, 2.5) follows an order-parameter-like behaviour with a transition temperature T_N = 151 K and a critical exponent β = 0.24 ± 0.03. **d**, Magnetic Bragg peaks at T = 3.6 K at $\mathbf{Q}$ = (0, 0.5, L), where the background measured at T = 201 K has been subtracted. **e**, L-dependence of the magnetic excitation intensity at 60 ± 10 meV, exhibiting a pronounced bilayer periodic modulation. Similar behaviour was also observed at low energies (Supplementary Fig. 7). The intensity follows $I(q_x, q_y, q_z, \omega) = I_0(q_x, q_y, q_z, \omega)\sin^2(q_z d/2)$, where d is the distance between adjacent NiO_2 layers. **f**, Energy dependence of low-energy spin excitations at $\mathbf{Q}$ = (0, 0.5, 2.5), revealing a spin gap of ~5 meV. The incoherent background away from the magnetic signal has been subtracted. The inelastic data were collected with ARCS, and the elastic data were collected with TOPAN. Error bars in **c**–**f** represent one standard deviation (±1σ) propagated from neutron counting statistics. $\mathbf{Q}$ = (H, K, L) denotes the momentum-transfer vector; q_x, q_y and q_z are its components along the reciprocal-space directions; ω is the energy transfer; and $I_0(q_x, q_y, q_z, \omega)$ is the intensity envelope excluding the bilayer-interference factor. mb, millibarns; f.u., formula unit; rlu, reciprocal lattice units.

https://doi.org/10.1038/s41563-026-02768-3

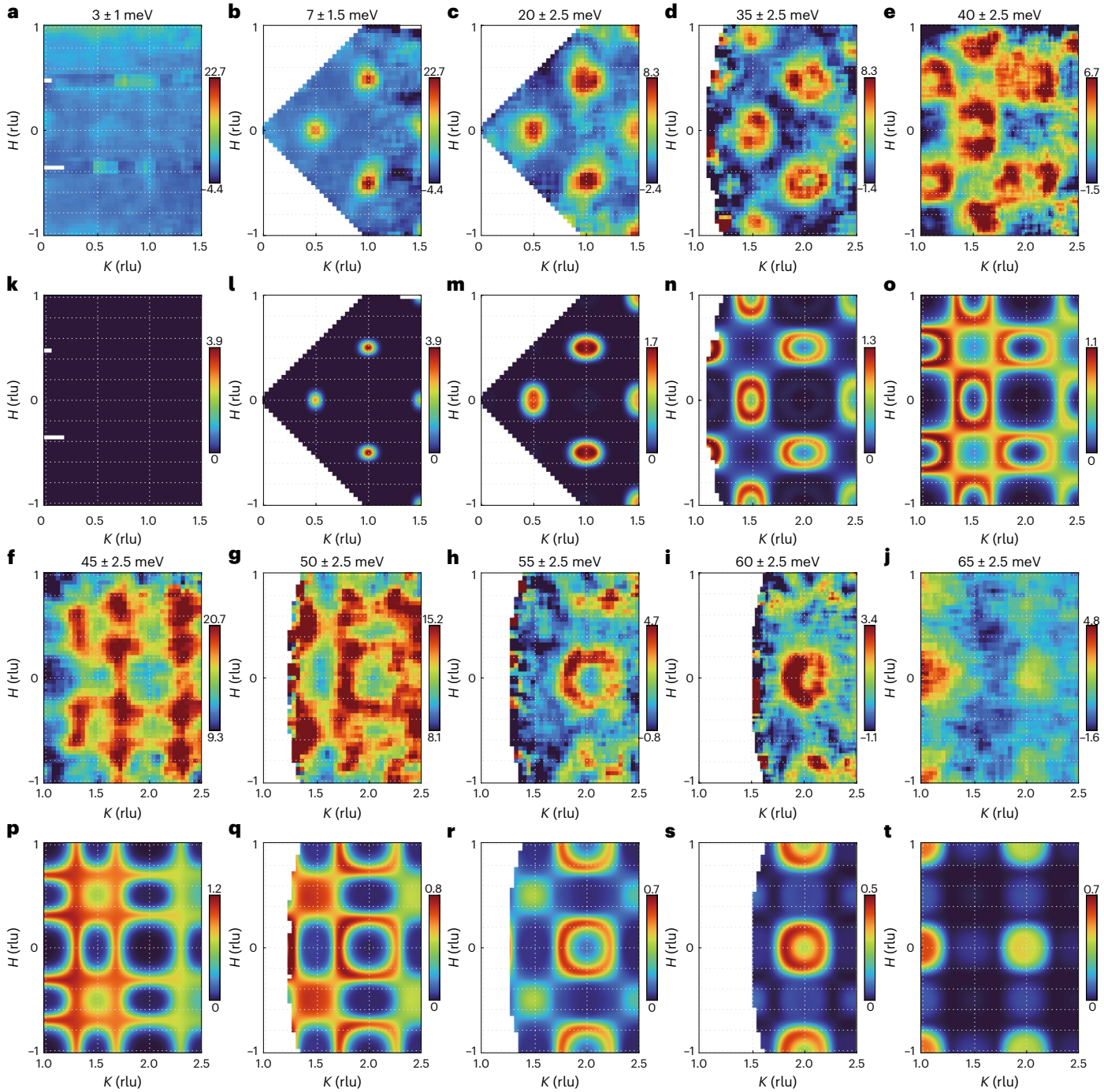


Fig. 2 | Momentum dependence of the spin excitations in $La_3Ni_2O_7$. **a**–**j**, Constant-energy slices of the magnetic excitations measured at $T = 6$ K, integrated over energies of 3 ± 1 meV (**a**), 7 ± 1.5 meV (**b**), 20 ± 2.5 meV (**c**), 35 ± 2.5 meV (**d**), 40 ± 2.5 meV (**e**), 45 ± 2.5 meV (**f**), 50 ± 2.5 meV (**g**), 55 ± 2.5 meV (**h**), 60 ± 2.5 meV (**i**) and 65 ± 2.5 meV (**j**). The |**Q**|-dependent isotropic background has been subtracted using an approach like that in ref. 53 for all panels except **f** and **g**, where the signals are broad and raw data are, therefore, shown. In **f** and **g**, a moderately enhanced background at large |**Q**| originates from the phonon scattering background. The measurements were performed with ARCS with incident neutron energies of 20 meV (**a**, **b**), 60 meV (**d**) or 120 meV (**c** and **e**–**j**). Symmetry-equivalent data were collected and averaged to improve statistical accuracy. **k**–**t**, Simulated constant-energy slices of the magnetic excitations, corresponding to the energy slices and reciprocal-space regions shown in **a**–**j**: 3 ± 1 meV (**k**), 7 ± 1.5 meV (**l**), 20 ± 2.5 meV (**m**), 35 ± 2.5 meV (**n**), 40 ± 2.5 meV (**o**), 45 ± 2.5 meV (**p**), 50 ± 2.5 meV (**q**), 55 ± 2.5 meV (**r**), 60 ± 2.5 meV (**s**) and 65 ± 2.5 meV (**t**). The colour scale for the experimental data is in units of mb meV^{-1} sr^{-1} $f.u.^{-1}$, whereas that for the simulated slices is in arbitrary units.

which provides an ideal foundation for determining the precise magnetic structure and exchange interactions. The intensity of the (0, 0.5, 2.5) peak as a function of temperature indicates the onset of magnetic order at 151 K and aligns with the susceptibility measurements (Fig. 1c). The elastic neutron diffraction intensity observed at **Q** = (0, 0.5, 0.5) and equivalent positions can, in principle, be explained by either a stripe- or a double-stripe-type magnetic structure, both characterized by antiferromagnetic alignment between adjacent bilayers, as the two models yield similar magnetic structure factors (Fig. 1a,b and Supplementary Fig. 4a).

To further resolve the magnetic ground state and interactions, we carried out inelastic neutron scattering measurements. Figure 2

https://doi.org/10.1038/s41563-026-02768-3

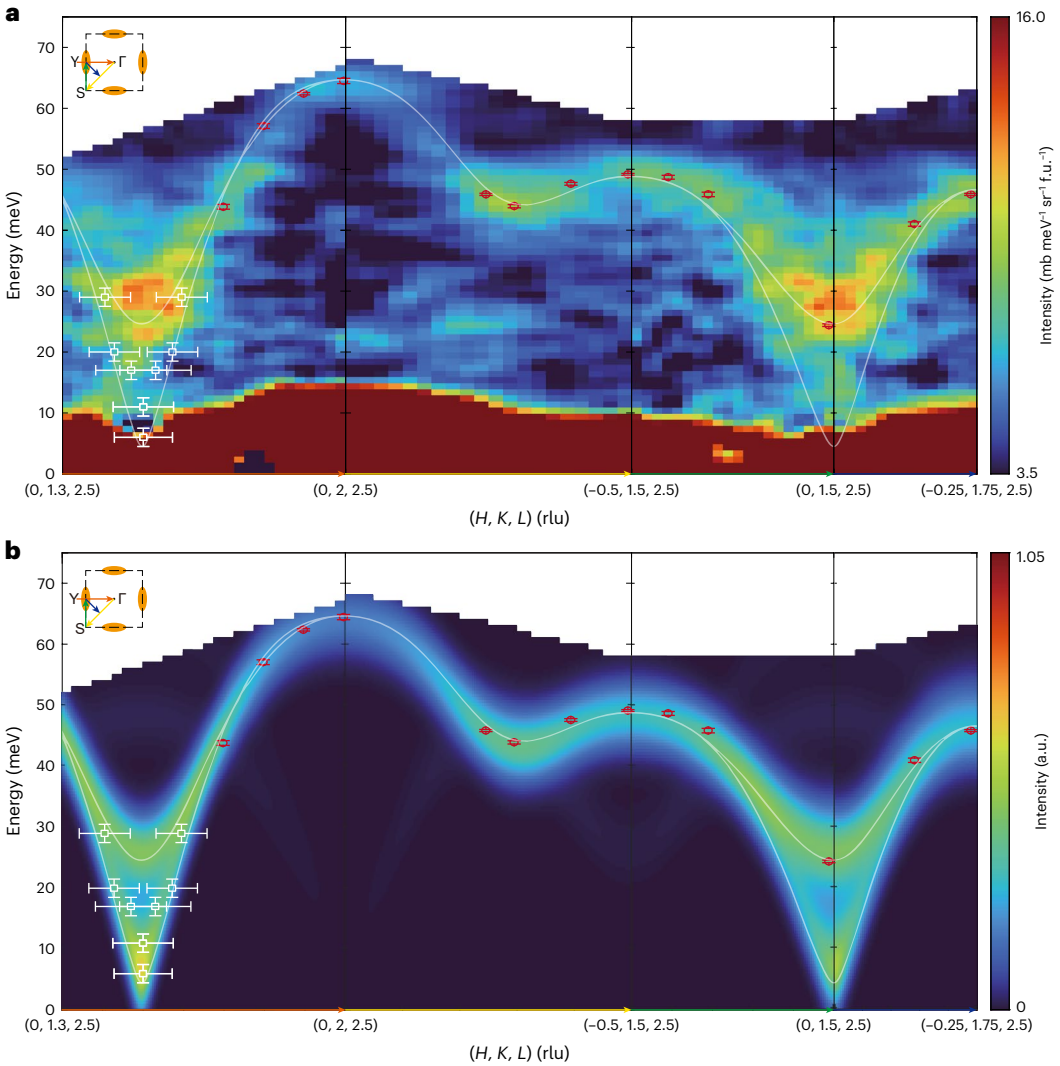


Fig. 3 | Measured and calculated spin-wave dispersions in $La_3Ni_2O_7$ at T = 6 K. **a**, Background-subtracted intensity map of the spin-excitation spectrum along the high-symmetry momentum directions (indicated by the arrows in the inset). The background was subtracted using the Shiver procedure. **b**, Simulated spin-excitation dispersion over the same region of reciprocal space as shown in **a**. The white solid lines denote the calculated dispersion relation. Red circles mark peak positions determined from fits for energy cuts (Supplementary Fig. 3). White squares indicate the peak positions extracted from Fig. 4c–g. For the white squares, the vertical bars indicate the energy integration ranges, and the horizontal bars represent the full-widths at half-maximum obtained from the fits. For the red circles, the error bars indicate 1σ uncertainties from the fit. The enhanced low-energy intensity below 10 meV in the measured spectra arises from incoherent scattering associated with the elastic line for incident energy E_i = 120 meV. Data were collected with ARCS.

displays constant-energy maps of the spin excitations in the (H,K,2.5) plane of reciprocal space, acquired at 6 K, well below the magnetic ordering temperature. The excitations are centred at $\mathbf{Q}$ = (0.5 ± n, 0 ± m, 2.5) and $\mathbf{Q}$ = (0 ± n, 0.5 ± m, 2.5), where n and m are integers. Although the underlying lattice symmetry is orthorhombic with the space group *Amam*, the presence of 90° twin domains, arising from the nearly equivalent lattice constants a and b, leads to a four-fold-like symmetry of the magnetic excitations. Energy cuts through the excitation signal revealed a spin gap of about 5 meV (Fig. 1f), consistent with the constant-energy maps (Fig. 2a,b). The finite gap reflects an appreciable magnetic anisotropy, consistent with the easy-axis orientation along the a direction. It therefore provides another low-energy scale that constrains the spin dynamics beyond the dominant exchange interactions.

With increasing energy (Fig. 2a–j), the excitations at (0, 0.5, 2.5) disperse outwards anisotropically, with a steeper dispersion along the K direction than along H, forming an elliptical ring at ~35 meV. Along the H direction, the excitations merge with those from the neighbouring Brillouin zone at around 49 meV, producing a square-like pattern (Fig. 2f,g). At higher energies, the signal forms a ring at (0, 2, 2.5) and eventually reaches the band top near 70 meV (Fig. 2h–j).

To better visualize the dispersion in energy–momentum (E–$\mathbf{Q}$) space, we projected the excitations along high-symmetry paths. As shown in Fig. 3a, the dispersion along (0, 1.3, 2.5) → (0, 2, 2.5) corresponds to the steeper branch, whereas the path (−0.5, 1.5, 2.5) → (0, 1.5, 2.5) follows the flatter branch and highlights pronounced zone-boundary softening. The combination of softening and anisotropic dispersion is indicative of underlying competing magnetic interactions, as we discuss later. Another branch near (0, 1.5, 2.5) was resolved with a gap of around 25 meV.

To quantify the dispersions and intensities of the spin excitations, we performed constant-energy cuts at various energies. As shown in Fig. 4a–g, the single peak centred at (0, 0.5, 2.5) at 6 meV evolves into a pair of peaks along the K direction for $E \geq 20$ meV. Similar behaviour was observed for cuts along the H direction, albeit with a more gradual dispersion, consistent with the anisotropy revealed in the constant-energy images and E–$\mathbf{Q}$ plots (Figs. 2 and 3).

https://doi.org/10.1038/s41563-026-02768-3

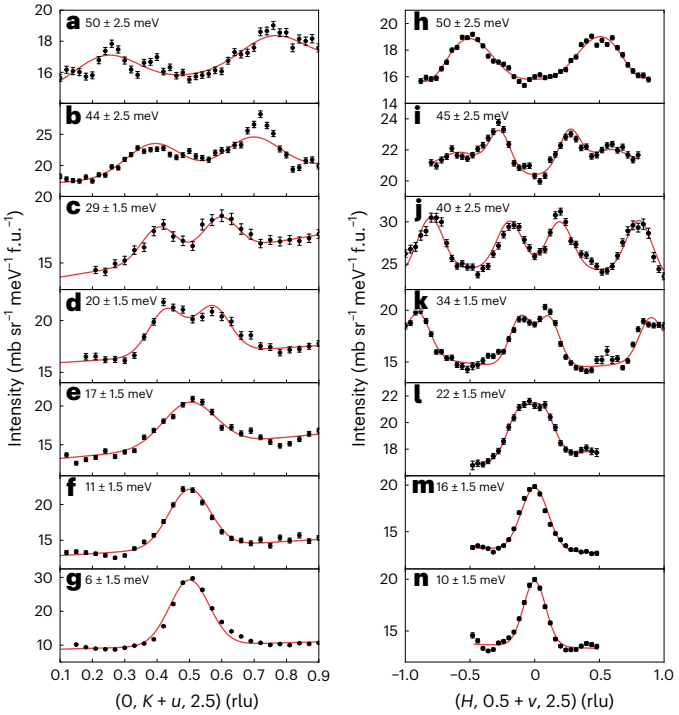


Fig. 4 | Constant-energy cuts of the spin excitations in $La_3Ni_2O_7$. a–g, Constant-energy cuts of the spin excitation along the *K* direction at 6 K for the indicated energies: 50 ± 2.5 meV (**a**), 44 ± 2.5 meV (**b**), 29 ± 1.5 meV (**c**), 20 ± 1.5 meV (**d**), 17 ± 1.5 meV (**e**), 11 ± 1.5 meV (**f**) and 6 ± 1.5 meV (**g**). The parameter $u = 1$ for **a** and **b** and $u = 0$ for **c**–**g**. **h**–**n**, Constant-energy cuts along the *H* direction at 6 K: 50 ± 2.5 meV (**h**), 45 ± 2.5 meV (**i**), 40 ± 2.5 meV (**j**), 34 ± 1.5 meV (**k**), 22 ± 1.5 meV (**l**), 16 ± 1.5 meV (**m**) and 10 ± 1.5 meV (**n**). The parameter $v = 1$ for **h**–**k** and $v = 0$ for **l**–**n**. Error bars in all panels represent one standard deviation ($\pm 1\sigma$) propagated from neutron counting statistics. Data were collected with ARCS.

Having established the in-plane momentum dependence of the spin excitations, we next examined their out-of-plane behaviour by performing cuts along the *L* direction. The excitation intensity exhibited pronounced *L*-dependent modulations, consistent with bilayer periodicity and providing direct evidence for antiferromagnetic interlayer spin correlations (Fig. 1e and Supplementary Fig. 7). The spectral weight was dominated by the acoustic branch, which showed a sine-like modulation and reached its maximum near $L \approx 2.6$ (Fig. 1e and Supplementary Fig. 7), whereas the optical branch remained much less intense and was resolved as a feature at the complementary position near $L \approx 5.2$ (Supplementary Fig. 8).

To quantitatively elucidate the magnetic interactions underlying the gapped, anisotropic in-plane spin-excitation dispersion together with the interlayer correlations in $La_3Ni_2O_7$, we carried out a systematic analysis within the framework of a Heisenberg-type Hamiltonian (Fig. 1a,b). The model Hamiltonian can be expressed as:

$$H = \sum_i J_c \mathbf{S}_i^{\mathrm{t}} \cdot \mathbf{S}_i^{\mathrm{b}} + \sum_{\langle i,j \rangle} J_2 \mathbf{S}_i^{\alpha} \cdot \mathbf{S}_j^{\alpha} + \sum_{\langle i,j \rangle_a} J_{1a} \mathbf{S}_i^{\alpha} \cdot \mathbf{S}_j^{\alpha}$$
$$+ \sum_{\langle i,j \rangle_b} J_{1b} \mathbf{S}_i^{\alpha} \cdot \mathbf{S}_j^{\alpha} + \sum_i A(\mathbf{S}_i \cdot \mathbf{n})^2$$

Here α denotes the layer index for the top (t) or bottom (b) layer. $\mathbf{S}_i^{\alpha}$ is the spin operator at magnetic Ni site *i* in layer α. J_c is the interlayer exchange interaction, and J_2 is the next-nearest-neighbour exchange coupling. J_{1a} and J_{1b} represent the nearest-neighbour exchange couplings along the *a* and *b* directions, respectively. *A* denotes the single-ion anisotropy and **n** denotes a unit vector along the *a* axis (Fig. 1a,b). This minimal Hamiltonian does not include an explicit coupling between neighbouring bilayers. Although the half-integer *L* dependence of the elastic magnetic peaks shows that adjacent bilayers are antiferromagnetically phased, the energy scale selecting this interbilayer phase relation is expected to be much smaller than the dominant intrabilayer and in-plane interactions. The microscopic origin of this weak phasing interaction is beyond the scope of the present minimal model and may involve a weak residual interbilayer exchange or subtle lattice distortions that lift the geometrical frustration.

Using the SpinW package, we simulated with linear spin-wave theory the spin-excitation spectra along high-symmetry directions, systematically varying the interaction parameters to capture the experimental dispersions. As an initial attempt, we employed a model containing only in-plane exchange interactions (Supplementary Fig. 6). This model reproduced a low-energy branch near (0, 0.5, 2.5) but incorrectly predicted further low-energy intensity at (0, 1, 2.5), inconsistent with its experimental identification as a zone boundary. The pronounced *L*-dependent intensity modulation with bilayer periodicity indicates the necessity of including substantial antiferromagnetic interlayer coupling. Indeed, only by introducing a sizeable interlayer exchange J_c could these discrepancies be resolved, underscoring the critical role of interlayer correlations in $La_3Ni_2O_7$.

Because the previously proposed single-stripe and double-stripe spin configurations yield nearly identical magnetic wavevectors and static structure factors, it is difficult to unambiguously differentiate them with elastic scattering alone. Inelastic neutron scattering, with momentum- and energy-resolved spectra over the entire Brillouin zone, provides a sensitive fingerprint of the underlying spin configuration. In comparative spin-wave simulations, the double-stripe model yielded an almost isotropic in-plane dispersion, in clear disagreement with the data (Figs. 2a–j and 3a and Supplementary Fig. 4). Introducing in-plane anisotropic exchanges or further neighbour couplings in the double-stripe model induced some dispersion anisotropy, but the resulting intensity distribution contradicted experimental observations (Fig. 2a–j and Supplementary Fig. 5c–j). Moreover, this model also predicted further low-energy branches near the zone centre that are not observed (Fig. 3a and Supplementary Fig. 5b). By contrast, the single-stripe configuration naturally reproduced the observed characteristics: the pronounced in-plane anisotropy and the softening of the zone-boundary excitation near (0.5, 0.5, 2.5), both originating from competing magnetic interactions between intra- and interstripe antiferromagnetic couplings. With optimized exchange coupling parameters $SJ_c = 39.86 \pm 0.85$, $SJ_{1a} = 2.36 \pm 0.22$, $SJ_{1b} = 3.71 \pm 0.44$, $SJ_2 = 4.63 \pm 0.18$ and $SA = -0.07 \pm 0.015$ meV, the calculated dispersions quantitatively reproduced the measured spectra. Here, *S* denotes the spin magnitude, and the quoted uncertainties represent the statistical uncertainties within the adopted stripe-type linear spin-wave fit. Possible systematic effects associated with background subtraction and model choice are not included. The simulations captured not only the overall bandwidth and energy scale but also the subtle momentum dependence along high-symmetry directions (Fig. 3a,b). Moreover, the computed constant-energy maps reproduced the anisotropic elliptical scattering features observed experimentally (Fig. 2). Within the present spin-wave framework, the fitted parameters are tightly constrained by these momentum- and energy-resolved features and provide a consistent description of the dominant magnetic interactions.

In the effective spin-wave description, the stripe spin order, consisting of alternating magnetic and non-magnetic stripes and breaking the in-plane C_4 symmetry, can be stabilized by the relatively strong next-nearest-neighbour antiferromagnetic coupling J_2 along the diagonal direction (Fig. 1b). The nearest-neighbour antiferromagnetic exchange J_{1b} promotes antiferromagnetic alignment between adjacent spin stripes, whereas the weaker antiferromagnetic coupling J_{1a} between parallel-aligned spins within a stripe introduces magnetic frustration. This frustration or competing interaction gives rise to the observed softening of the transverse spin-wave branch and the

https://doi.org/10.1038/s41563-026-02768-3

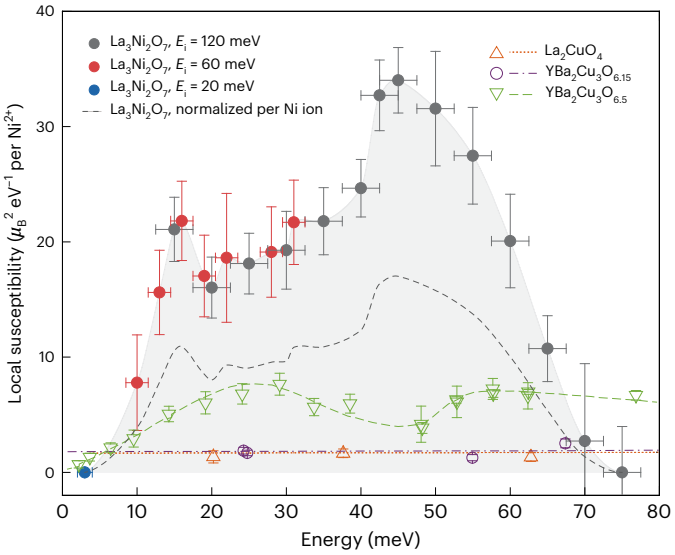


Fig. 5 | Energy dependence of the local dynamic susceptibility $\chi''(\omega)$ in $La_3Ni_2O_7$. Blue, red and black circles are from measurements with incident energies E_i = 20 meV, 60 meV and 120 meV at 6 K, respectively. The data were integrated over $1 < L < 6.2$ rlu, covering approximately one full bilayer-modulation period and including both acoustic and optical magnetic signals. The low- and mid-energy spectral weight was measured with several incident energies, and only data points that were mutually consistent between different E_i settings and free from identifiable phonon or sample-environment contamination were used to construct $\chi''(\omega)$. The horizontal bars represent the energy integration ranges, and the vertical bars denote the statistical uncertainties, representing one standard deviation ($\pm1\sigma$) propagated from neutron counting statistics. The shaded area shows $\chi''(\omega)$ normalized per magnetic Ni^{2+} site in the stripe model. The dashed grey curve shows the same spectrum rescaled per total planar Ni site. In the nominal mixed-valence stripe picture, half of the Ni sites carry sizeable magnetic moments, so this curve is smaller by a factor of two. The inelastic neutron scattering data were collected with ARCS. The cuprate data points were extracted from the literature and normalized per planar Cu ion. Open triangles and circles denote cuprate parent compounds measured at 295 K (refs. 54,55). Open inverted triangles denote the normal state of the $YBa_2Cu_3O_{6.5}$ superconductor at 60 K (ref. 56). For $YBa_2Cu_3O_{6.15}$ and $YBa_2Cu_3O_{6.5}$, the acoustic and optical branches are summed.

pronounced in-plane anisotropy. The strong interlayer exchange J_c originates from superexchange interactions mediated by apical oxygens associated with the d_{z^2} orbitals between adjacent NiO_2 layers, where the Ni–Ni distance is relatively short. This exchange hierarchy contrasts with that of bilayer cuprates. In bilayer $YBa_2Cu_3O_{6+x}$, acoustic and optical spin waves are described by an in-plane exchange $J_{ab} \approx 125$ meV and an intrabilayer exchange $J_c \approx 11$ meV, so the bilayer coupling is much weaker than the in-plane exchange[45–47]. In $La_3Ni_2O_7$, by contrast, SJ_c is one of the largest magnetic energy scales, larger than the effective in-plane couplings, revealing a reversed bilayer-to-in-plane exchange hierarchy.

Analysis of the elastic neutron diffraction data yielded an ordered magnetic moment of $0.67(3)\mu_B$ per ordered Ni ion in the single-stripe model, where μ_B is the Bohr magneton, which is substantially smaller than that expected in the ionic limit for a fully localized $S = 1$ system, consistent with the presence of competing magnetic interactions and, possibly, also with the influence of Ni–O covalency and electronic itinerancy. These results suggest that a bilayer Heisenberg model with a delicately balanced interplay of strong interlayer coupling and competing in-plane interactions, together with a single-stripe spin configuration, may provide a consistent description of the spin order and dynamics in $La_3Ni_2O_7$.

Further insight into the nature of magnetic correlations and their implications for superconductivity could be obtained from the energy dependence of local dynamic susceptibility, transformed into absolute units by normalization to the acoustic phonons. This procedure enables a direct, quantitative comparison with cuprates, other superconductors and theoretical models. As shown in Fig. 5, in addition to a spin gap below ~5 meV, the absolute local dynamic susceptibility exhibited a continuum of mid-energy spin excitations within 10–70 meV. By integrating the magnetic signal over energy and including the elastic ordered contribution, we obtained a total magnetic spectral weight of $1.75 \pm 0.25\mu_B^2$ per ordered Ni^{2+} on the stripe, corresponding to $0.88 \pm 0.13\ \mu_B^2$ per total planar Ni site, comparable with that of cuprates. As electronic itinerancy typically suppresses the dynamic magnetic moment, the persistence of a considerable fluctuating moment indicates that itinerant electrons coexist with local magnetism in $La_3Ni_2O_7$, sustained by substantial electron correlations. For context, the insulating single-layer nickelate $La_{2-x}Sr_xNiO_4$ also exhibits well-defined spin waves[48,49]. The key distinction in bilayer $La_3Ni_2O_7$ is that stripe-type in-plane correlations coexist with strong intrabilayer antiferromagnetic coupling and acoustic and optical spin-wave branches, revealing a bilayer magnetic framework absent in the single-layer nickelates.

Although the total fluctuating moments of both systems are comparable, the overall spin-excitation bandwidth in $La_3Ni_2O_7$ is limited to ~70 meV, far smaller than the ~300 meV bandwidth of cuprates. Because the change in bandwidth is rather small between the bulk $La_3Ni_2O_7$ and the superconducting phase under compressive strain[32,35], the fluctuation moment and overall spin-excitation spectra are expected to remain comparable between the parent and superconducting states, in accordance with the magnetic moment sum rule. Yet the superconducting critical temperatures of nickelates and cuprates are of similar magnitudes. This contrast indicates that a large spin-excitation bandwidth is not, by itself, the decisive ingredient for pairing. Rather, the density and character of spin fluctuations near the relevant electronic energy scales seem to be key. Indeed, the absolute local dynamic susceptibility in the 10 meV to 70 meV range is markedly larger in $La_3Ni_2O_7$ than in cuprates (Fig. 5), suggesting that these dense mid-energy spin excitations couple more effectively to electrons on the energy scale relevant to Cooper pairing.

In $La_3Ni_2O_7$, these relevant energy scales may arise from two complementary channels. The first is the interlayer coupling between adjacent Ni ions, mediated by apical oxygens and dominated by the d_{z^2} orbital. This coupling may directly produce excitations with energies of the same order as the superconducting gap[44,50–52]. Second, intralayer exchange interactions within the NiO_2 planes, although individually modest, combine to produce collective excitation energies up to about 30–40 meV, again comparable with the gap[44,50–52] (Supplementary Fig. 6). These excitations are mainly linked to the $d_{x^2-y^2}$ orbital and provide another reservoir of spectral weight. Such a unique combination of interlayer and intralayer interactions creates a high density of mid-energy spin excitations that are well matched to the pairing scale.

The quantitative determination of the magnetic interactions in $La_3Ni_2O_7$ provides important insight into the pressure- and strain-tuned magnetic phase diagram, as well as its relation to superconductivity. Within a local-moment framework, the in-plane magnetic interactions are sufficient to stabilize the single-stripe magnetic order. Moreover, the combination of sizeable interlayer coupling and competing in-plane exchange interactions places this magnetic state in a delicate balance, making it sensitive to external perturbations, such as pressure and in-plane strain. Under pressure or compressive epitaxial strain, $La_3Ni_2O_7$ is expected to undergo subtle structural changes, including a reduction of the in-plane orthorhombicity and a suppression of NiO_6 octahedral tilts. Such a higher-symmetry structure could reduce the lattice pinning of the stripe-type order and weaken the static magnetic order, while allowing strong dynamic spin correlations to persist. This suggests a scenario in which superconductivity emerges not from the loss of magnetic interactions but from a redistribution of the magnetic spectral weight from static order to fluctuating correlations. Within the

effective spin-wave description, these structural changes can also modify the balance among J_{1a},J_{1b},J_2 and J_c, providing a magnetic route by which pressure or strain tunes the competing interactions identified here. The involvement of both $d_{x^2-y^2}$ and d_{z^2} orbitals further suggests that superconductivity in bilayer nickelates is shaped by the cooperation of in-plane and interlayer magnetic correlations. The ability to grow large $La_3Ni_2O_7$ single crystals and determine their spin dynamics in absolute units provides a quantitative materials benchmark for understanding how structural tuning, orbital selectivity and magnetic spectral weight are linked in superconducting bilayer nickelates.

This work establishes a quantitative magnetic framework for $La_3Ni_2O_7$: a stripe-type magnetic ground state with competing in-plane interactions and strong antiferromagnetic interlayer coupling, effectively captured by a bilayer Heisenberg-type model. Although its spin-wave bandwidth is only about 25% of that in cuprates, $La_3Ni_2O_7$ exhibits an enhanced mid-energy local dynamic susceptibility and a comparable total fluctuating moment, reflecting robust electronic correlations and magnetic interactions persisting into its metallic state. The presence of intense mid-energy spin excitations, coupled with bilayer magnetism, outlines a new magnetic framework distinct from that of cuprates. Our findings suggest that the key to superconductivity in bilayer nickelates may not lie in achieving large spin-excitation bandwidths but rather in generating a dense spectrum of magnetic fluctuations concentrated near the pairing energy scale. The cooperative involvement of both $d_{x^2-y^2}$ and d_{z^2} orbitals, coupled through interlayer and intralayer exchange pathways, naturally provides such an environment, linking orbital selectivity and spin dynamics to the emergence of high-temperature superconductivity. By quantitatively establishing the absolute scale and character of spin order and dynamics in single-crystalline $La_3Ni_2O_7$, this work places stringent experimental constraints on theoretical models and provides a foundation for understanding pressure- and strain-induced superconductivity across this class of materials.

Online content

Any methods, additional references, Nature Portfolio reporting summaries, source data, extended data, supplementary information, acknowledgements, peer review information; details of author contributions and competing interests; and statements of data and code availability are available at https://doi.org/10.1038/s41563-026-02768-3.

References

1. Lee, P. A., Nagaosa, N. & Wen, X.-G. Doping a Mott insulator: physics of high-temperature superconductivity. *Rev. Mod. Phys.* **78**, 17–85 (2006).
2. Scalapino, D. J. A common thread: the pairing interaction for unconventional superconductors. *Rev. Mod. Phys.* **84**, 1383–1417 (2012).
3. Dai, P. Antiferromagnetic order and spin dynamics in iron-based superconductors. *Rev. Mod. Phys.* **87**, 855–896 (2015).
4. Sun, H. et al. Signatures of superconductivity near 80 K in a nickelate under high pressure. *Nature* **621**, 493–498 (2023).
5. Zhu, Y. et al. Superconductivity in pressurized trilayer $La_4Ni_3O_{10-\delta}$ single crystals. *Nature* **631**, 531–536 (2024).
6. Li, D. et al. Superconductivity in an infinite-layer nickelate. *Nature* **572**, 624–627 (2019).
7. Ko, E. K. et al. Signatures of ambient pressure superconductivity in thin film $La_3Ni_2O_7$. *Nature* **638**, 935–940 (2025).
8. Zhou, G. et al. Ambient-pressure superconductivity onset above 40 K in $(La, Pr)_3Ni_2O_7$ films. *Nature* **640**, 641–646 (2025).
9. Wang, M., Wen, H.-H., Wu, T., Yao, D.-X. & Xiang, T. Normal and superconducting properties of $La_3Ni_2O_7$. *Chin. Phys. Lett.* **41**, 077402 (2024).
10. Uchida, M. et al. Pseudogap-related charge dynamics in the layered nickelate $R_{2-x}Sr_xNiO_4$ ($x \sim 1$). *Phys. Rev. B* **86**, 165126 (2012).
11. Ikeda, Y. et al. Inelastic neutron scattering study of stripe and overdoped checkerboard ordering in layered nickel oxide $Nd_{2-x}Sr_xNiO_4$. *J. Phys. Soc. Jpn* **85**, 023701 (2016).
12. LaBollita, H. Assessing spin-density wave formation in $La_3Ni_2O_7$ from electronic structure calculations. *Phys. Rev. Mater.* **8**, L111801 (2024).
13. Wú, W., Luo, Z., Yao, D.-X. & Wang, M. Superexchange and charge transfer in the nickelate superconductor $La_3Ni_2O_7$ under pressure. *Sci. China Phys. Mech. Astron.* **67**, 117402 (2024).
14. Ni, X.-S. et al. Spin density wave in the bilayered nickelate $La_3Ni_2O_{7-\delta}$ at ambient pressure. *npj Quantum Mater.* **10**, 17 (2025).
15. Zhang, B., Xu, C. & Xiang, H. Spin-charge-orbital order in nickelate superconductors. *Phys. Rev. B* **111**, 184401 (2025).
16. Liu, Y.-B. et al. Origin of the diagonal double-stripe spin density wave and potential superconductivity in bulk $La_3Ni_2O_7$ at ambient pressure. *Phys. Rev. B* **112**, 014510 (2025).
17. Luo, Z., Hu, X., Wang, M., Wú, W. & Yao, D.-X. Bilayer two-orbital model of $La_3Ni_2O_7$ under pressure. *Phys. Rev. Lett.* **131**, 126001 (2023).
18. Shen, Y., Qin, M. & Zhang, G.-M. Effective bi-layer model Hamiltonian and density-matrix renormalization group study for the high-T_c superconductivity in $La_3Ni_2O_7$ under high pressure. *Chin. Phys. Lett.* **40**, 127401 (2023).
19. Yang, Y., Zhang, G.-M. & Zhang, F.-C. Interlayer valence bonds and two-component theory for high T_c superconductivity of $La_3Ni_2O_7$ under pressure. *Phys. Rev. B* **108**, L201108 (2023).
20. Zhang, Y., Lin, L.-F., Moreo, A. & Dagotto, E. Electronic structure, dimer physics, orbital-selective behavior, and magnetic tendencies in the bilayer nickelate superconductor $La_3Ni_2O_7$ under pressure. *Phys. Rev. B* **108**, L180510 (2023).
21. Liao, Z. et al. Electron correlations and superconductivity in $La_3Ni_2O_7$ under pressure tuning. *Phys. Rev. B* **108**, 214522 (2023).
22. Qu, X.-Z. et al. Bilayer t-J-$J_\perp$ model and magnetically mediated pairing in the pressurized nickelate $La_3Ni_2O_7$. *Phys. Rev. Lett.* **132**, 036502 (2024).
23. Sakakibara, H., Kitamine, N., Ochi, M. & Kuroki, K. Possible high T_c superconductivity in $La_3Ni_2O_7$ under high pressure through manifestation of a nearly half-filled bilayer Hubbard model. *Phys. Rev. Lett.* **132**, 106002 (2024).
24. Lu, C., Pan, Z., Yang, F. & Wu, C. Interlayer-coupling-driven high-temperature superconductivity in $La_3Ni_2O_7$ under pressure. *Phys. Rev. Lett.* **132**, 146002 (2024).
25. Bötzel, S., Lechermann, F., Gondolf, J. & Eremin, I. M. Theory of magnetic excitations in the multilayer nickelate superconductor $La_3Ni_2O_7$. *Phys. Rev. B* **109**, L180502 (2024).
26. Fan, Z. et al. Superconductivity in nickelate and cuprate superconductors with strong bilayer coupling. *Phys. Rev. B* **110**, 024514 (2024).
27. Xia, C., Liu, H., Zhou, S. & Chen, H. Sensitive dependence of pairing symmetry on Ni-e_g crystal field splitting in the nickelate superconductor $La_3Ni_2O_7$. *Nat. Commun.* **16**, 1054 (2025).
28. Jiang, K.-Y., Cao, Y.-H., Yang, Q.-G., Lu, H.-Y. & Wang, Q.-H. Theory of pressure dependence of superconductivity in bilayer nickelate $La_3Ni_2O_7$. *Phys. Rev. Lett.* **134**, 076001 (2025).
29. Xi, W., Yu, S.-L. & Li, J.-X. Transition from $s^{\pm}$-wave to $d_{x^2-y^2}$-wave superconductivity driven by interlayer interaction in the bilayer two-orbital model of $La_3Ni_2O_7$. *Phys. Rev. B* **111**, 104505 (2025).
30. Gu, Y., Le, C., Yang, Z., Wu, X. & Hu, J. Effective model and pairing tendency in the bilayer Ni-based superconductor $La_3Ni_2O_7$. *Phys. Rev. B* **111**, 174506 (2025).
31. Li, F. et al. Bulk superconductivity up to 96 K in pressurized nickelate single crystals. *Nature* **649**, 871–878 (2026).
32. Chen, X. et al. Electronic and magnetic excitations in $La_3Ni_2O_7$. *Nat. Commun.* **15**, 9597 (2024).
33. Gupta, N. K. et al. Anisotropic spin stripe domains in bilayer $La_3Ni_2O_7$. *Nat. Commun.* **16**, 6560 (2025).

34. Ren, X. et al. Resolving the electronic ground state of $La_3Ni_2O_{7-\delta}$ films. *Commun. Phys.* **8**, 52 (2025).
35. Zhong, H. et al. Spin correlations in $La_3Ni_2O_7$ superconducting thin films. Preprint at https://arxiv.org/abs/2502.03178 (2025).
36. Chen, K. et al. Evidence of spin density waves in $La_3Ni_2O_{7-\delta}$. *Phys. Rev. Lett.* **132**, 256503 (2024).
37. Zhao, D. et al. Pressure-enhanced spin-density-wave transition in double-layer nickelate $La_3Ni_2O_{7-\delta}$. *Sci. Bull.* **70**, 1239–1245 (2025).
38. Khasanov, R. et al. Pressure-enhanced splitting of density wave transitions in $La_3Ni_2O_{7-\delta}$. *Nat. Phys.* **21**, 430–436 (2025).
39. Misawa, R. et al. Polar, checkerboard charge order in bilayer nickelate $La_3Ni_2O_7$. Preprint at https://arxiv.org/abs/2603.25119v1 (2026).
40. Xie, T. et al. Strong interlayer magnetic exchange coupling in $La_3Ni_2O_{7-\delta}$ revealed by inelastic neutron scattering. *Sci. Bull.* **69**, 3221–3227 (2024).
41. Ling, C. D., Argyriou, D. N., Wu, G. & Neumeier, J. J. Neutron diffraction study of $La_3Ni_2O_7$: structural relationships among n=1, 2, and 3 phases $La_{n+1}Ni_nO_{3n+1}$. *J. Solid State Chem.* **152**, 517–525 (2000).
42. Plokhikh, I. et al. Unraveling spin density wave order in layered nickelates $La_3Ni_2O_7$ and $La_2PrNi_2O_7$ via neutron diffraction. *Phys. Rev. Res.* **8**, 033151 (2026).
43. Le Tacon, M. et al. Intense paramagnon excitations in a large family of high-temperature superconductors. *Nat. Phys.* **7**, 725–730 (2011).
44. Cao, Z.-Y. et al. Direct observation of d-wave superconducting gap symmetry in pressurized $La_3Ni_2O_{7-\delta}$ single crystals. Preprint at https://arxiv.org/abs/2509.12606 (2025).
45. Reznik, D. et al. Direct observation of optical magnons in $YBa_2Cu_3O_{6.2}$. *Phys. Rev. B* **53**, R14741–R14744 (1996).
46. Pailhès, S. et al. Resonant magnetic excitations at high energy in superconducting $YBa_2Cu_3O_{6.85}$. *Phys. Rev. Lett.* **93**, 167001 (2004).
47. Woo, H. et al. Magnetic energy change available to superconducting condensation in optimally doped $YBa_2Cu_3O_{6.95}$. *Nat. Phys.* **2**, 600–604 (2006).
48. Boothroyd, A. T. et al. Spin dynamics in stripe-ordered $La_{5/3}Sr_{1/3}NiO_4$. *Phys. Rev. B* **67**, 100407 (2003).
49. Woo, H. et al. Mapping spin-wave dispersions in stripe-ordered $La_{2-x}Sr_xNiO_4$ (x=0.275, 0.333). *Phys. Rev. B* **72**, 064437 (2005).
50. Liu, C. et al. Andreev reflection in superconducting state of pressurized $La_3Ni_2O_7$. *Sci. China Phys. Mech. Astron.* **68**, 247412 (2025).
51. Guo, J. et al. Revealing superconducting gap in $La_3Ni_2O_{7-\delta}$ by Andreev reflection spectroscopy under high pressure. *Nat. Commun.* **16**, 10838 (2025).
52. Fan, S. et al. Single-particle tunneling spectrum with a robust superconducting gap in $La_2PrNi_2O_7$ thin films at ambient pressure. *Sci. Adv.* **12**, eaeg2429 (2026).
53. Wang, Q. et al. Magnetic ground state of FeSe. *Nat. Commun.* **7**, 12182 (2016).
54. Hayden, S. M. et al. Comparison of the high-frequency magnetic fluctuations in insulating and superconducting $La_{2-x}Sr_xCuO_4$. *Phys. Rev. Lett.* **76**, 1344–1347 (1996).
55. Hayden, S. M., Aeppli, G., Perring, T. G. & Mook, H. A. High-frequency spin waves in $YBa_2Cu_3O_{6.15}$. *Phys. Rev. B* **54**, R6905 (1996).
56. Bourges, P. et al. High-energy spin excitations in $YBa_2Cu_3O_{6.5}$. *Phys. Rev. B* **56**, R11439–R11442 (1997).

Publisher's note Springer Nature remains neutral with regard to jurisdictional claims in published maps and institutional affiliations.

Springer Nature or its licensor (e.g. a society or other partner) holds exclusive rights to this article under a publishing agreement with the author(s) or other rightsholder(s); author self-archiving of the accepted manuscript version of this article is solely governed by the terms of such publishing agreement and applicable law.

© The Author(s), under exclusive licence to Springer Nature Limited 2026

Methods

Growth and characterization of $La_3Ni_2O_7$ single crystals

The polycrystalline precursor of $La_3Ni_2O_7$ was synthesized via a conventional solid-state reaction. High-purity La_2O_3 and NiO powders (Aladdin, 99.99%) were weighed in stoichiometric proportions, thoroughly ground and subsequently calcined at 1,400 K for 24 h. We conducted another cycle of grinding and calcination to ensure homogeneity. The resulting powder was then hydrostatically pressed into a cylindrical rod (approximately 6 mm in diameter and 10 cm in length) under a pressure of 300 MPa. The rod was sintered at 1,400 K for 12 h in air so that it attained sufficient density and mechanical strength for the crystal growth process. Single-crystal growth was carried out in a vertical optical floating-zone furnace (Model HKZ, SciDre) under an oxygen pressure of 14–16 bar using a 5-kW xenon arc lamp as the heat source. The feed rod was translated through the molten zone at a rate of 5 mm h^{-1}.

Phase purity and crystal structure were verified by X-ray diffraction (Cu–Kα radiation, D8 Discover diffractometer, Bruker; Supplementary Fig. 1). Magnetic and transport properties were characterized using Quantum Design MPMS-3 SQUID magnetometer and Physical Property Measurement System. Zero-field-cooled magnetization measurements between 2 K and 300 K revealed antiferromagnetic ordering below ~151 K. The resistivity exhibited metallic behaviour with a clear anomaly near the magnetic transition temperature (Supplementary Fig. 1). Thermogravimetric analysis was performed on NETZSCH STA 449F3 and STA 449F1 instruments (Supplementary Fig. 11). Chemical compositions were analysed by an energy-dispersive X-ray spectrometer attached to a field-emission scanning electron microscope (Sigma 300, Zeiss) (Supplementary Fig. 10).

Neutron scattering experiments

Inelastic neutron scattering measurements were performed with the ARCS spectrometer at Oak Ridge National Laboratory and the MAPS spectrometer at the ISIS Neutron and Muon Facility. Twenty-five $La_3Ni_2O_7$ single crystals, with a total mass of ~1.26 g, were co-aligned in the (O, K, L) scattering plane. Experiments with ARCS were conducted in a closed-cycle refrigerator down to 6 K using incident energies E_i = 20 meV, 60 meV, 120 meV and 200 meV. Experiments on MAPS were performed in a closed-cycle refrigerator from 6 K to 300 K with E_i = 40 meV, 60 meV, 100 meV, 120 meV, 180 meV and 200 meV. The magnetic scattering intensities were placed on an absolute scale by normalization to acoustic phonons, enabling absolute calibration of the imaginary part of the dynamic susceptibility $\chi''(\omega)$ and allowing quantitative comparison with that of cuprates and other superconductors. Data reduction and analysis were performed using the HORACE and Shiver software packages, which we used to slice and project the four-dimensional dataset into (H, K, L, E) space.

The elastic neutron scattering experiment was performed using the triple-axis spectrometer TOPAN installed at the 6-G horizontal beam port of the Japan Research Reactor 3 (JRR-3). We used neutrons with an energy of 13.4 meV. A vertically focusing pyrolytic graphite monochromator and analyser were employed. The collimation was set to blank-60′-60′-60′. To suppress higher-order contamination, pyrolytic graphite filters were placed in front of both the monochromator and the analyser. The sample was mounted on an aluminium plate using CYTOP and sealed in an aluminium can together with helium exchange gas. The sample was cooled using a water-cooled Gifford–McMahon refrigerator, and measurements were carried out in a temperature range of approximately 3.6 K to 200 K.

Data availability

Source data are provided with this paper.

Acknowledgements

We thank M. Okawara and G. Takahashi for technical assistance at JRR-3. A portion of this research used resources at the Spallation Neutron Source, a DOE Office of Science User Facility operated by the Oak Ridge National Laboratory. The neutron diffraction experiments were performed under the Joint-Use Research Program for Neutron Scattering, Institute for Solid State Physics, University of Tokyo, at JRR-3 (6G IRT programme 25402), and the GIMRT research programme of the Institute for Materials Research, Tohoku University (202508-QBKNE-0507). Some of the measurements were performed using the facilities of the Fudan Nano-fabrication Laboratory.

Author contributions

J.Z. conceived and supervised the project. L.C., E.Z. and Y.Z. synthesized the single-crystal samples. L.C., E.Z., B.C., F.L. and W.W. characterized the samples. L.C., E.Z., Y.Z. and H.Z. performed the inelastic neutron scattering measurements with support from D.L.A. and T.J.W. Y.I. and L.C. performed the elastic neutron scattering measurements. L.C., Y.H., W.W., Q.W. and J.Z. analysed the data. J.Z. and L.C. wrote the paper. All authors provided comments for the Article.

Funding

This work was supported by the Key Program of the National Natural Science Foundation of China (12234006), the Shanghai Municipal Science and Technology Project (25DZ3008100 and 2019SHZDZX01), the National Key R&D Program of China (2022YFA1403202), the Quantum Science and Technology and National Science and Technology Major Project (2024ZD0300103) and the Large Scientific Facility Open Subject of Songshan Lake Laboratory (DG23313511). Y.Z. was supported by the Youth Foundation of the National Natural Science Foundation of China (12304173). Q.W. acknowledges support from the Research Grants Council of Hong Kong (ECS No. 24306223).

Competing interests

The authors declare no competing interests.

Additional information

Supplementary information The online version contains supplementary material available at https://doi.org/10.1038/s41563-026-02768-3.

Correspondence and requests for materials should be addressed to Jun Zhao.

Peer review information *Nature Materials* thanks the anonymous reviewers for their contribution to the peer review of this work.

Reprints and permissions information is available at www.nature.com/reprints.